Loss mechanisms in resonant spectrophones

Ralph H. Johnson, Robert Gerlach, Launey J. Thomas III, and Nabil M. Amer

Quality factors and resonant frequencies of a resonant spectrophone have been measured as a function of pressure and the results compared to theoretical predictions which took into account classical surface and volumetric losses and molecular relaxation. Buffer gases investigated included the five noble gases, H_2, N_2, O_2, CO_2, N_2O, and SF_6. Typically 95% of the cavity losses were accounted for theoretically. Frequency shifts due to relaxational dispersion, nonideal gas behavior, and classical boundary layer effects were observed; all behaved as predicted by theory.

I. Introduction

In studies of gas-phase photoacoustic spectroscopy and detection, the gas whose spectrum is being investigated is generally one of several present in the sample, and often it is only present in trace amounts. The response of the spectrophone is determined by the characteristics of the sample gas as a whole and depends on the various thermal and molecular relaxational properties of the gases present. In particular, for an acoustically resonant spectrophone, important parameters will include the sound velocity, heat capacity, thermal conductivity, viscosity, and the energies and relaxation times of the molecular vibrations. The sound velocity determines the resonant frequencies of the cavity, while the other parameters govern the loss mechanisms that determine the quality factors of the resonances and also cause small shifts in the resonant frequencies. In an earlier study,[1] the resonant frequencies and quality factors of acoustical resonances were determined for various buffer gases at atmospheric pressure, and the results were compared to theoretical predictions from classical acoustics. For all gases studied, the cavity losses were significantly larger than predicted, with the largest discrepancies occurring for the polyatomic gases, for which molecular relaxation is expected to be important. It is the goal of this work to investigate the damping mechanisms in the resonant spectrophone systematically, including their pressure dependence, and to incorporate molecular relaxation effects into the theoretical interpretation of the results.

II. Theory

For a cylindrical cavity the resonant frequency of mode mnp is given by[2]

$$f_{mnp} = \frac{c}{2}\left[\left(\frac{\alpha_{mn}}{R}\right)^2 + \left(\frac{p}{L}\right)^2\right]^{1/2},\qquad(1)$$

where c is the sound velocity; R and L are the cavity radius and length; m, n, and p are the azimuthal, radial, and longitudinal mode numbers, respectively; and

$$\alpha_{mn} = n\text{th zero of } \frac{dJ_m(\pi\alpha)}{d\alpha}.$$

Equation (1) assumes that there is no phase shift on reflection of the pressure wave from the cavity walls either due to wall compliance or boundary layer effects. We will retain the assumption of complete wall rigidity, but it will be seen that the boundary layer causes significant frequency deviations from the above formula. Also, in evaluating the frequency from Eq. (1), one must remember that the sound velocity c may vary with frequency and pressure due to molecular relaxation effects and nonideal behavior of the gas.

The two major categories of damping are surface damping and volumetric damping. Surface damping may be due to[3] (1) compliance of the chamber walls, (2) dissipation at the microphone diaphragm, (3) scattering at surface imperfections, or (4) viscous and thermal dissipation in the boundary layer at the smooth internal surfaces.

The first three effects are minimized by suitable design of the spectrophone. The fourth loss mechanism is then dominant, and for purely radial modes its contribution to the cavity Q is given by[3]

$$\frac{1}{Q^{cl}_{\text{surf}}} = \frac{1}{L}\left[d_v + (\gamma - 1)d_h\left(1 + \frac{L}{R}\right)\right],\qquad(2)$$

where $d_v = (2\eta/\rho\omega)^{1/2}$ and $d_h = (2\kappa M/\rho C_p\omega)^{1/2}$ are the viscous and thermal boundary layer thicknesses, η is the

shear viscosity, κ is the thermal conductivity, M is the mass per mole, C_p is the molar heat capacity, and $\gamma = C_p/C_v$.

The volumetric losses may be due to[3] (1) free space viscous and thermal dissipation, (2) diffusion effects, (3) radiation effects, and (4) relaxational damping. The damping due to free space viscous and thermal dissipation (Stokes-Kirchhoff) is small when compared with surface damping, but in some extreme cases at low pressure it can become significant. The contribution of free space viscous and thermal dissipation to the Q is given by[4]

$$\frac{1}{Q_{\text{vol}}^{cl}} = \frac{\omega}{\gamma p}\left[\frac{4}{3}\eta + (\gamma - 1)\frac{\kappa M}{C_p}\right].$$
(3)

No bulk viscosity term was included, since bulk viscosity is synonymous with molecular relaxation effects,[4] which will be treated separately.

Diffusion and radiation effects are very small.[3]

Relaxational effects arise because of the finite time required for the internal degrees of freedom of the molecules to come into thermal equilibrium with their environment, as expressed by the equation[4]

$$\frac{dE_n}{dt} = -\frac{1}{\tau_n}(E_n - E_n^e),$$

where E_n is the ensemble average of the energy in the nth mode of the molecule, E_n^e is its equilibrium value, and τ_n is the relaxation time for that mode. A harmonic sound wave carries with it a temperature variation which causes the equilibrium energy E_n^e to vary harmonically with time; solution of the above differential equation then leads us to the dynamic heat capacity $C_n(\omega)$ for the nth mode:

$$C_n(\omega) = \frac{C_n}{1 + i\omega\tau_n},$$
(4)

where C_n is the static heat capacity, i.e., $C_n(0)$. Then, considering all degrees of freedom, we have

$$C_v(\omega) = C_v + \sum_n [C_n(\omega) - C_n],$$
(5)

$$C_p(\omega) = C_p + \sum_n [C_n(\omega) - C_n],$$
(6)

for the dynamic heat capacities at constant volume and pressure, respectively, where C_v and C_p are the static heat capacities. Using Eqs. (4)–(6) we then find the dynamic specific heat ratio:

$$\gamma(\omega) = \frac{C_p - \sum_n C_n i\omega\tau_n/(1 + i\omega\tau_n)}{C_v - \sum_n C_n i\omega\tau_n/(1 + i\omega\tau_n)}.$$
(7)

In general the resonant frequency of a mode is given by Eq. (1), which contains a leading factor of c, the sound velocity. Neglecting nonideal gas effects, which can be treated separately, $c = [\gamma(\omega)p/\rho]^{1/2}$. If we denote by ω_0 the frequency we would obtain for the mode by using the static specific heat ratio γ in place of $\gamma(\omega)$, in general

$$\omega = \omega_0\left[\frac{\gamma(\omega)}{\gamma}\right]^{1/2}.$$
(8)

Using Eq. (7), we obtain

$$\omega = \frac{\omega_0}{\gamma^{1/2}}\frac{[(A^2 + B^2 + R'B)^2 + A^2R'^2]^{1/4}}{(A^2 + B^2)^{1/2}}\exp(i\Psi/2),$$
(9)

where

$$A = \sum_n \frac{C_n \sin\phi_n}{(1 + \omega^2\tau_n^2)^{1/2}},$$

$$B = C_v + \sum_n C_n\left[\frac{\cos\phi_n}{(1 + \omega^2\tau_n^2)^{1/2}} - 1\right],$$

$$R' = C_p - C_v,$$

$$\Psi = \tan^{-1}\left[\frac{-AR'}{A^2 + B^2 + R'B}\right],$$

$$\phi_n = \tan^{-1}(-\omega\tau_n).$$

Equation (9) appears to be an implicit equation for ω in terms of itself, since A, B, etc. are functions of ω. However, the dispersion is small enough that one may substitute ω_0 for ω without significant loss of accuracy. The resonant frequency is then given by

$$\omega_{\text{res}} = \text{Re}\,\omega,$$
(10)

while the contribution of the relaxational losses to the Q of the resonance is given by

$$\frac{1}{Q_{\text{rel}}} = \frac{2\,\text{Im}\,\omega}{\omega_0}.$$
(11)

For many molecular gases the entire vibrational heat capacity can be considered to relax with a single relaxation time.[5] In that case Eq. (9) simplifies mainly in the elimination of summations in the definitions of A and B.

Another important special case is that of many separately relaxing levels with short relaxation times such that $\omega_0\tau_n \ll 1$. For such a case, Eq. (9) simplifies to

$$\omega \cong \omega_0\left[1 + i\frac{\omega_0}{2}\left(\frac{\gamma - 1}{C_p}\right)\sum_n \tau_n C_n\right].$$
(12)

The contribution of the relaxational losses to the Q is then given by

$$\frac{1}{Q_{\text{rel}}} \cong \omega_0\left(\frac{\gamma - 1}{C_p}\right)\sum_n \tau_n C_n.$$
(13)

There is no dispersion to first order in $\omega_0\tau_n$.

In all the above expressions, the relaxation times τ_n appear in conjunction with ω as a product $\omega\tau_n$. Although there are various effects that shift the frequency of the resonance, such as relaxational dispersion, virial shifts, and boundary layer effects, it is still true that the frequency of a given resonance is nearly independent of pressure for the gases and pressure range considered here, the largest observed frequency shift being ∼10% and most others much smaller. Therefore, observation of the dependence of the Q and resonant frequency on pressure will mainly reflect the pressure dependence of τ_n. Since, at constant temperature, the product of pressure and relaxation time is constant, observation of the pressure dependence of the Q and resonant frequency provides a means of determining the $p\tau$ product.[6] Although we loosely use the term relaxation time
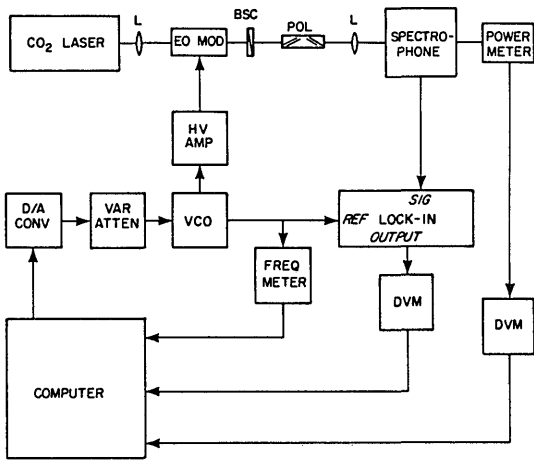
Fig. 1. Block diagram of the experimental setup.

to denote one of the parameters of our experiment, what is always meant is the $p\tau$ product, generally expressed in atm sec.

The overall Q factor for a resonance may be found by summing all the losses for that resonance, expressed as $1/Q_i$:

$$\frac{1}{Q_{\text{tot}}} = \sum_i \frac{1}{Q_i} . \qquad (14)$$

In practice we include only three contributions: $1/Q_{\text{surf}}^{cl}$; $1/Q_{\text{vol}}^{cl}$; and $1/Q_{\text{rel}}$.

The specific heat ratio appears in the expressions for $1/Q_{\text{surf}}^{cl}$ and $1/Q_{\text{vol}}^{cl}$. Care must be taken to use a value of γ appropriate for the pressure and frequency being considered, namely, the real part of the dynamic $\gamma(\omega)$ from Eq. (7).

Before discussing the experiment, we mention two sources of shifts in the resonant frequency in addition to the relaxational dispersion discussed above.

The losses due to the boundary layers arise from the real, or resistive, part of the boundary layer specific acoustic impedance. That impedance also has an imaginary, or reactive, part which gives rise to phase shifts on reflection. These phase shifts will give rise to changes in the frequency of a standing wave in the cavity. Such boundary layer shifts have been calculated and observed for acoustically excited spherical resonators.[7] The physical interpretation of the thermal boundary layer's contribution to the frequency shift is easy to see. In the bulk of the gas, sound propagates adiabatically with a velocity $(\gamma p/\rho)^{1/2}$. The gas in the boundary layer, however, is in good thermal contact with the walls, and, therefore, as one approaches the wall, the sound velocity approaches its isothermal value $(p/\rho)^{1/2}$. This reduction in sound velocity in the boundary layer is like an increase in the dimensions of the resonator and produces a downward shift in frequency. The viscous boundary layer shift, while less intuitively obvious, is generally of comparable magnitude. We show in the Appendix that for a radial mode of a cylindrical resonator the boundary layer shift is given by

$$\left(\frac{\delta\omega}{\omega}\right)_{b.l.} = -\frac{1}{2L}\left[d_v + (\gamma - 1)d_h\left(1 + \frac{L}{R}\right)\right] , \qquad (15)$$

where we have adopted the sign convention that a positive $\delta\omega$ represents an increase in frequency. Since d_v and d_h go as $(\rho\omega)^{-1/2}$, the shift is most pronounced at low pressures and for low frequency resonances. The magnitude of the shift is exactly equal to the contribution of the boundary layer losses to the halfwidth of the resonance.

Another source of frequency shifts is the variation of the speed of sound with pressure due to the nonideal behavior of the gas. This shift is given by[8]

$$\left(\frac{\delta\omega}{\omega}\right)_{\text{vir}} = \frac{p}{R_g T}\left[B + \frac{T}{h}\frac{dB}{dT} + \frac{T^2}{2h(h+1)}\frac{d^2B}{dT^2}\right] , \qquad (16)$$

where B is the second virial coefficient, $h = C_v/R_g$, and R_g is the gas constant.

III. Experiment

The basic experimental arrangement is shown in Fig. 1. The CO_2 laser was grating tuned and emitted 2–4 W/line. A standard electrooptic modulation system consisting of a CdTe Pockels cell, CdS Babinet-Soleil compensator, and ZnSe Brewster plate polarizer was employed.

The modulator was driven by a high voltage amplifier which began rolling off at ~10 kHz but was still useful up to 25 kHz at decreased modulation depth. The input to the amplifier came from a voltage controlled oscillator whose frequency was controlled by a computer via a digital-to-analog converter (DAC) and a variable attenuator; the latter was used so that resonances of varying width could be scanned through without varying the output range of the DAC. A frequency meter monitored the VCO frequency and fed it back to the computer.

The spectrophone was constructed of stainless steel to reduce outgassing problems. The cell was cylindrical with a diameter of 15.489 cm and a length of 15.446 cm; the choice of $2R \cong L$ minimized the ratio of surface area to volume for a fixed volume. The diameter was uniform to within 0.0013 cm, and the ends were parallel to within 0.0013 cm. Great care was taken to minimize the perturbations to the cylindrical cavity geometry. The windows, mounted at the centers of the end plates, were nearly flush with the walls, recessed by only 0.013 cm. The Knowles BT-1759 miniature electret microphone was mounted in the cylinder wall halfway between the ends. A 0.476-cm diam hole was made for the microphone face, which was recessed by 0.013 cm from the wall. The valve for introducing gas into the cell was an integral part of the end plate, and the valve stem tip was flush with the wall when the valve was closed and was visually indistinguishable from the rest of the wall. It was located at the node of the first radial mode. All internal surfaces, including the valve stem tip, were polished to a finish which was smooth to within less than the smallest boundary layer thickness to be encountered in the experiment, so that the boundary layers would have a well-defined geometry, and their losses could be calculated accurately. The end plates were smooth to

(%)		(%)		(%)	
He	99.999	Xe	99.9995	CO_2	99.995
Ne	99.999	H_2	99.9999	N_2O	99.998
Ar	99.998	N_2	99.9995	SF_6	99.99
Kr	99.995	O_2	99.9995		

within 0.2-μm rms, while the cylinder walls were smooth to within 0.5 μm generally but had some 20-μm scratches.[9]

The end plates were sealed with Viton O rings. The windows and microphone were sealed with Techkits E-7, an epoxy with good vacuum properties.[10] While the epoxy limited the bakeout temperature of the spectrophone, the higher temperature epoxies we tried did not seal well to the NaCl windows.

A thermistor mounted in the wall of the spectrophone allowed temperature readings accurate to ±0.1 K.

The microphone signal was fed to a two-phase lock-in amplifier whose vector magnitude output was measured with a digital voltmeter and fed to the computer.

The laser power was measured with a thermopile and DVM and was used for signal normalization.

Prior to taking data, a standard bake-out procedure was performed on the gas mixing system, while the spectrophone itself was heated to 40°C, limited by the epoxy used for windows and microphone. When the outgassing rate decreased sufficiently the system was allowed to cool, and if the outgassing rate at room temperature was such that the impurities introduced by outgassing in the course of one set of data taking runs would be of the same order of magnitude as the impurities already present in the gas, the bakeout was considered adequate.

Gas mixing was performed in a cylindrical stainless steel chamber of volume equal to that of the spectrophone. This chamber had a dish machined in the bottom of it for a Teflon covered mixing rod, which was propelled by a magnetic stirrer external to the system. Most of the remainder of the gas mixing system was constructed of stainless steel. Validyne variable reluctance pressure gauges were used to measure pressures during gas mixing, while thermocouple gauges were used for measuring outgassing rates.

The object of the gas mixing process was to produce a mixture of 50 ppm of ethylene in each of the various buffer gases investigated. The ethylene was needed to give some absorption at CO_2 laser wavelengths. (No ethylene was added to SF_6, since it already absorbed strongly.) Mixing was accomplished with a double dilution procedure. The magnetic stirrer was used to mix the gases thoroughly. The entire mixing process generally took ~2 h.

A listing of the purities of the buffer gases used appears in Table I.

A data taking run proceeded by introducing the gas mixture into the spectrophone in small increments and scanning through the resonances at each pressure,

starting from typically ~10 Torr and proceeding upward to atmospheric pressure, then reversing the procedure and pumping the gas out of the spectrophone in small increments and either repeating measurements at previously studied pressures or filling in gaps at other pressures. The lowest pressure that could be studied was determined by noise considerations. Generally only the first radial mode was scanned at each pressure, but at atmospheric pressure a number of other modes were examined. It was possible to excite modes mnp having values of m (the azimuthal mode index) of 0 and 1 and all values of n (the radial mode index). The $m = 1$ modes were much more weakly excited than those with $m = 0$, and the fact that they were observed at all was apparently due to the beam being slightly off center. Except for the strong absorber SF_6, no modes having longitudinal dependence ($p \neq 0$) were observed except under unusual circumstances which will be discussed later. Often a particular mode would be scanned several times at the same pressure to assess the reproducibility. Measurements were made at ambient temperature, which ranged from 294 to 300 K but was typically around 298 K.

IV. Results

Curve fitting of the signal vs frequency data was performed on a CDC 7600 computer using a nonlinear least squares fitting program called MINUIT. The data were fit with the function

$$y(f) = A\left\{\left[\frac{2gf^2}{(f_r^2 - f^2)^2 + 4g^2f^2} - C_1\right]^2 + \left[\frac{(f_r^2 - f^2)f}{(f_r^2 - f^2)^2 + 4g^2f^2} - C_2\right]^2\right\}^{1/2} + C_3, \quad (17)$$

where the fitted parameters were A, f_r, g, C_1, C_2, and C_3. The parameters A, f_r, and g were, respectively, the amplitude, resonant frequency, and halfwidth. The parameters C_1 and C_2 were included to allow for zero
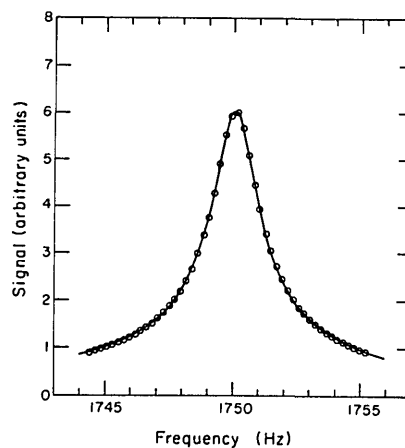

Fig. 2. Example of data points and fitted curve for first radial resonance of Kr at 760 Torr.

offsets in the two channels of the lock-in. The parameter C_3 was included to allow for a zero offset in the output of the vector adder. The experimental Q was found from

$$Q_{\text{exp}} = f_r/2g. \qquad (18)$$

An example of a set of data and fitted curve for the first radial resonance of Kr at 760 Torr is presented in Fig. 2. The curves fit very well for the high signal, low noise cases, with a typical rms deviation of 0.5% of the maximum amplitude. For low signal cases the deviation increased, but the fitting routine was sometimes still able to obtain meaningful numbers. Curve fitting greatly reduced the random error in the Q values relative to those obtained by finding the half-power points by interpolation.

The buffer gases studied fall into three categories: monatomic (He, Ne, Ar, Kr, Xe); diatomic (H_2, N_2, O_2); and polyatomic gases (CO_2, N_2O, SF_6).

A. Monatomic Gases

The noble gases provide an excellent opportunity to test the accuracy of the classical theory alone, since molecular relaxation effects are absent. In Fig. 3 we present the ratio of experimental to theoretical quality factor, $Q_{\text{exp}}/Q_{\text{theor}}$, for the first radial mode as a function of pressure for each of the five noble gases. Except at the lowest pressures, where the low SNR limited the accuracy of the Q determination, most of the values of the ratio lie in the range between 0.9 and 1.0 with a typical value being 0.95. Thus the classical losses, and in fact for all practical purposes the classical surface losses, come very close to accounting for all the losses. As one goes to higher radial modes at atmospheric pressure, the ratio $Q_{\text{exp}}/Q_{\text{theor}}$ decreases, with typical values for all the noble gases being 0.95, 0.90, and 0.85 for the first, second and fourth radial modes, respectively. The third radial mode is not easily characterized due to a mode coupling effect to be described below.

Since for a given mode the losses not accounted for appear to be a constant fraction of the calculated boundary layer losses, independent of pressure, it appears that these losses have the same pressure dependence as the boundary layer losses and may in fact be due to a boundary layer effect that appears in a higher order of perturbation theory. As one goes to higher frequency resonances, the higher order effects become more important because the density of other modes to which the boundary layer can couple a mode increases.

We have also observed the pressure dependence of the resonant frequency for the first radial mode, as shown in Fig. 4. Although negligible temperature variation occurred during the time required to scan through one resonance at one pressure, significant variations occurred during the time required to cover the entire range of pressures. To compensate for this, each observed resonant frequency was multiplied by $(298 \text{ K}/T)^{1/2}$ to adjust it to the frequency that would have been observed for a temperature of 298 K, which was a typical median temperature. The data presented

in Fig. 4 have been adjusted in this way. The arrows on the right-hand side indicate the frequencies that would be predicted by Eq. (1) with the ideal gas sound velocity $(\gamma p/\rho)^{1/2}$. It is seen that for all the noble gases, the frequency is depressed from this value, with the greatest frequency shift occurring at low pressures. In addition,
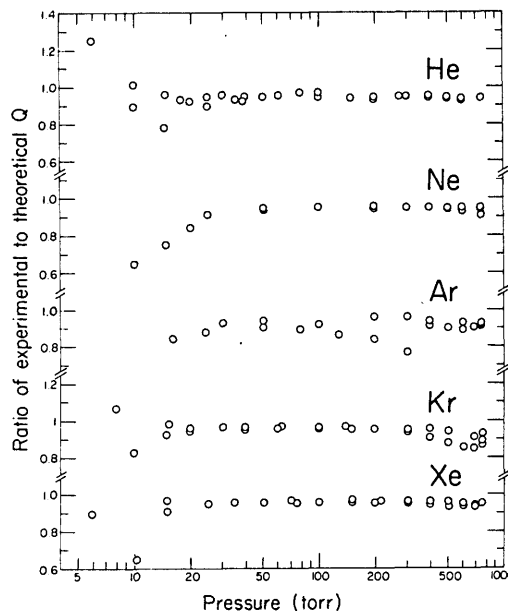

Fig. 3. Ratios of experimentally observed to theoretical quality factors vs pressure for the noble gases.
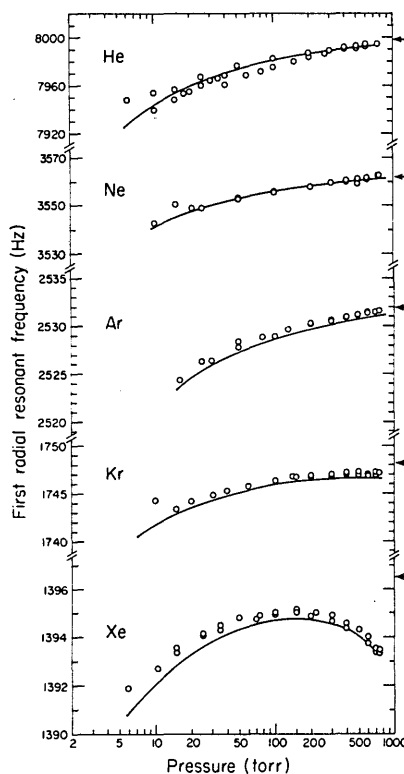

Fig. 4. First radial resonance frequency vs pressure for the noble gases. Arrows at the right indicate calculated frequencies assuming ideal gas with no boundary layer shift. Solid curves are calculated frequencies including virial and boundary layer shifts.
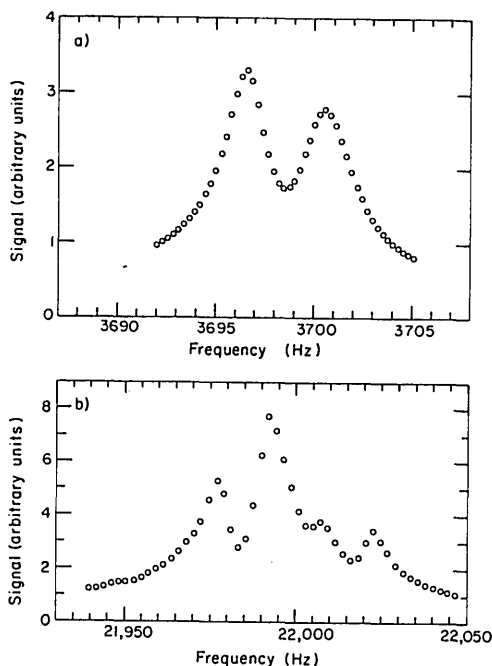
Fig. 5. Examples of mode coupling: (a) region of third radial mode of Xe at 760 Torr; (b) region of nineteenth radial mode of Xe at 760 Torr.

for Xe there is a considerable frequency decrease at high pressure. These effects are well explained by the boundary layer shift given by Eq. (18) and the virial shift given by Eq. (19).[11] The solid curves in Fig. 4 were obtained by adding these shifts to the frequency designated by the arrow. In all frequency vs pressure data that follow for other gases, these frequency shifts will have been subtracted out so as to isolate the frequency shifts due to molecular relaxation.

An interesting effect was observed for the third radial mode. For our particular value of the ratio R/L, this mode is very close to the frequency of the 016 radial-longitudinal mode. A double peak is observed in this frequency neighborhood, as shown in Fig. 5(a). Modes having longitudinal dependence are never excited directly in our experiment when they are remote from radial resonances. We believe, however, that since the 030 and 016 modes are so close in frequency, the perturbation due to the boundary layers, especially the viscous boundary layers on the end walls, produces a strong mixing of these modes, so that both resultant modes contain large admixtures of the 030 mode, which can be efficiently excited by the light beam even though the power deposited by the beam per unit length is uniform. From symmetry considerations, we only expect this boundary layer effect to couple radial modes to modes having even longitudinal mode number, a condition satisfied by the 016 mode.

As one goes to higher frequencies, the density of other modes to which coupling is possible increases rapidly, and very complicated looking resonances can be observed. An example is provided by Fig. 5(b), which shows the region of the nineteenth radial mode for Xe.

B. Diatomic Gases

In Fig. 6 we present the results for the three diatomic gases studied, H_2, N_2, and O_2. For each gas we present graphs of Q vs pressure and of frequency of the first radial mode (corrected for boundary layer and virial shifts and for temperature variations) vs pressure.

We discuss oxygen and nitrogen first. For these gases, as for the noble gases, the quality factor is again very close to the classical prediction [solid curves in Figs. 6(c) and (e)]. For low pressures ($\lesssim 100$ Torr) the ratio of the experimental to the classical theoretical Q is typically ~ 0.95 for both gases, the same as for the noble gases. However, as the pressure rises to atmospheric, Q_{exp}/Q_{theor}^{cl} falls off to 0.81 for O_2 and to 0.89 for N_2. This is apparently due to the onset of molecular relaxation effects. Since O_2 and N_2 both have very long relaxation times, the effect of relaxation does not become important until high pressures, and to get a good handle on the relaxation times, it is necessary to go considerably higher than we were able. We can make estimates, however, if we are careful not to try to make the relaxational losses account for the 5% unexplained losses which are observed even for noble gases and are apparently not relaxational in origin. We obtain relaxation times of 2 msec atm for O_2 and 0.3 msec atm for N_2, both considerably shorter than others have observed.[5] (It may seem surprising that a shorter relaxation time is obtained for N_2 than for O_2, although the effects of relaxation losses are less evident. This is because the vibrational heat capacity of nitrogen is so much smaller that it is necessary to employ a much shorter relaxation time to account for the losses.) It is known that oxygen vibrationally deexcites $\sim 10^4$ times more rapidly in collisions with methane than in collisions with other oxygen molecules,[5] and one might hypothesize that the ethylene is having a similar effect on both O_2 and N_2. However, we varied the ethylene concentration in O_2 between 0.25 and 50 ppm and found no significant change, so one must suppose that some other impurity is responsible for the short relaxation times observed.

The corrected frequencies of O_2 and N_2 are plotted with highly expanded frequency scales in Figs. 6(d) and (f), respectively. The arrows on the right-hand side indicate the frequencies calculated from Eq. (1) with $c = (\gamma p/\rho)^{1/2}$ and $\gamma = 1.4$, appropriate for low pressures where the vibrational heat capacity is inactive. Nearly all the O_2 frequencies fall within a 1-Hz band centered at this frequency, while the N_2 frequencies fall in a 1.5-Hz band which includes this frequency. The high pressure behavior of the N_2 data suggests that there was a small error in the virial correction applied.

For hydrogen, classical losses alone do not explain the observed Q values [Fig. 6(a)] at all well, especially at low pressures. Vibrational relaxation is negligible due to the extremely small vibrational heat capacity of H_2. Rotational relaxation, which for most gases is too rapid to contribute much damping at audio frequencies, is unusually slow in H_2, and since the first radial resonance occurs at a high frequency, the $\omega\tau$ products are fairly large, and rotational relaxation losses are significant. We have inserted rotational relaxation times from the

literature[12] into Eq. (16) to calculate the relaxational contribution to the losses. When we include this, we find good agreement with the data, as shown in Fig. 6(a).

The H_2 frequency data in Fig. 6(b) show a discrepancy between the points obtained for increasing pressure and those obtained for decreasing pressure, the latter occurring at lower frequencies. This discrepancy appears to be due to outgassing of a heavier gas, causing the sound velocity to decrease with time. (The outgassing is presumably of the last gas run before H_2, namely, SF_6, which, due to its high molecular weight, shifts the hydrogen resonant frequency downward by 0.38 Hz/ppm; thus even a small concentration of SF_6 will have a noticeable effect on the frequency.) This makes it somewhat difficult to determine whether the data show any unambiguous frequency shifts due to relaxational dispersion. Equation (12) indicates that no dispersion is predicted to first order in $\omega\tau$ or ω/p, so one would have to go to lower pressures to see dispersion than to see relaxation losses, which are first order in ω/p.

However, there is some hint of dispersion for the pressures below $\sim$50 Torr, particularly for the upper (less contaminated) curve. This is not surprising, since relaxation losses are significant even at atmospheric pressure, and since the amount of dispersion expected for H_2 if one could go low enough in pressure to obtain the entire dispersion curve is very large, 940 Hz, of which we are just seeing the first $\sim$10 Hz. Again the arrow indicates the frequency obtained from Eq. (1) with $c = (\gamma p/\rho)^{1/2}$ and $\gamma = 1.4028$.

C. Polyatomic Gases

Data for the polyatomic gases CO_2, N_2O, and SF_6 appear in Fig. 7, with the same format as for Fig. 6. For these gases vibrational relaxation is very important. For each gas, we assumed that the entire vibrational heat capacity relaxed with a single effective relaxation time, and we adjusted that one parameter to give the best fit to the frequency vs pressure data. The solid curves in Figs. 6(b), (d), and (f) are the fitted curves. (For N_2O, we could not go to low enough pressure with
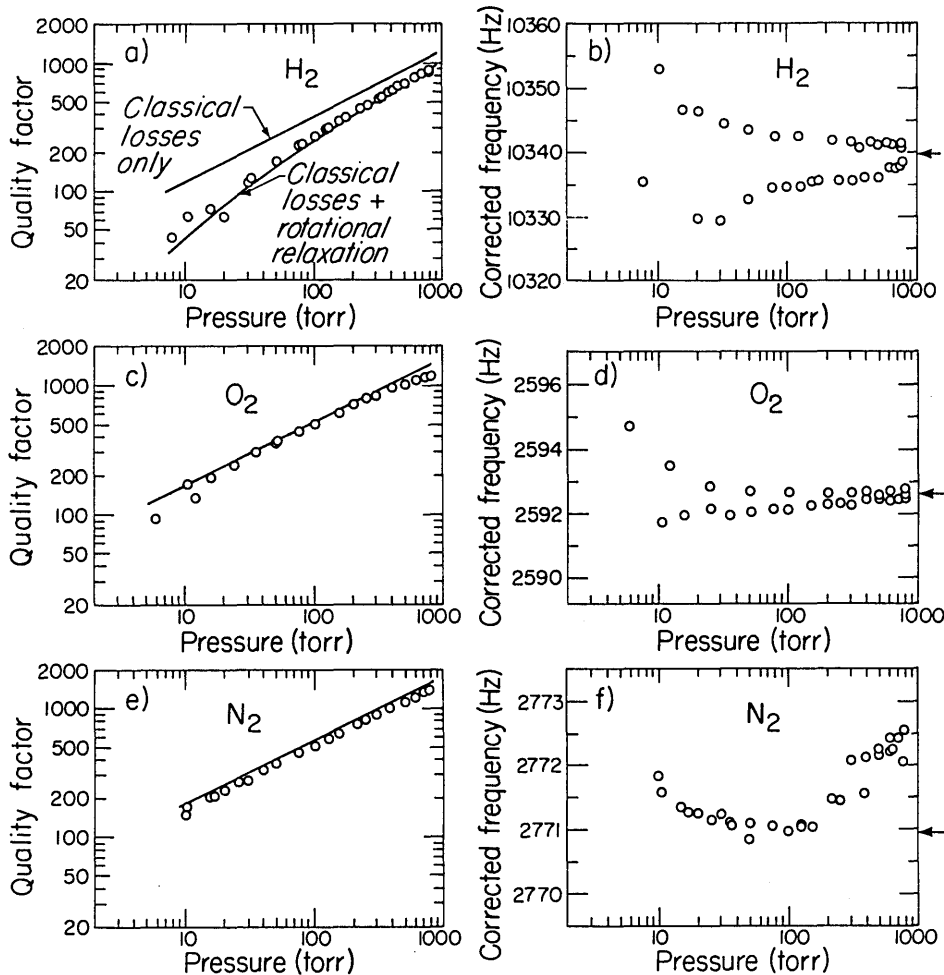

Fig. 6. Quality factor and first radial resonant frequency vs pressure for the diatomic gases. Frequencies have been corrected by subtracting out virial and boundary layer shifts. Arrows indicate calculated frequencies (see text). Solid curves for N_2 and O_2 plots of Q vs p represent classical losses only.

an adequate SNR to obtain the entire dispersion curve, but enough of the curve was obtained to pin down the relaxation time very well.) The relaxation time thus obtained was then used to calculate a theoretical Q vs pressure curve [solid curves in Figs. 7(a), (c), and (e)]. The agreement with the data for N_2O and SF_6 is very good. For CO_2 the predicted Q's are higher than those observed. This is not presently understood. An underestimate of the vibrational heat capacity due to neglect of anharmonic effects would have led to an underestimate of the relaxation losses, but also would have led to an underestimate of the amount of dispersion, which is clearly not the case in Fig. 7(b). The assumption of a single relaxation time is also not entirely responsible. Assuming two or more relaxation times might improve the shape of the Q vs pressure curve by broadening the minimum, but it would not bring it closer to the data. To do so requires a higher total vibrational heat capacity.

The vibrational relaxation times arrived at by curve fitting the frequency data were 2.8 μsec atm for CO_2, 0.94 μsec atm for N_2O, and 0.84 μsec atm for SF_6. The N_2O and SF_6 values agree fairly well with previously observed relaxation times of 0.99 and 0.76 μsec atm, respectively.[5] Again there is a discrepancy for CO_2, where a relaxation time of 7 μsec atm has been observed.[5] We hypothesize that the effect of the impurities on the relatively slowly relaxing CO_2 is more pronounced than on the faster relaxing N_2O and SF_6.

V. Conclusions

Loss mechanisms in resonant spectrophones were first considered quantitatively by Kamm,[3] who was able to account theoretically for 60% of the losses in his resonator. Later Thomas et al.[1] were able to account for typically ~80% of the losses for nonrelaxing gases and a considerably smaller percentage for the relaxing gases, using only classical effects to account for the losses.
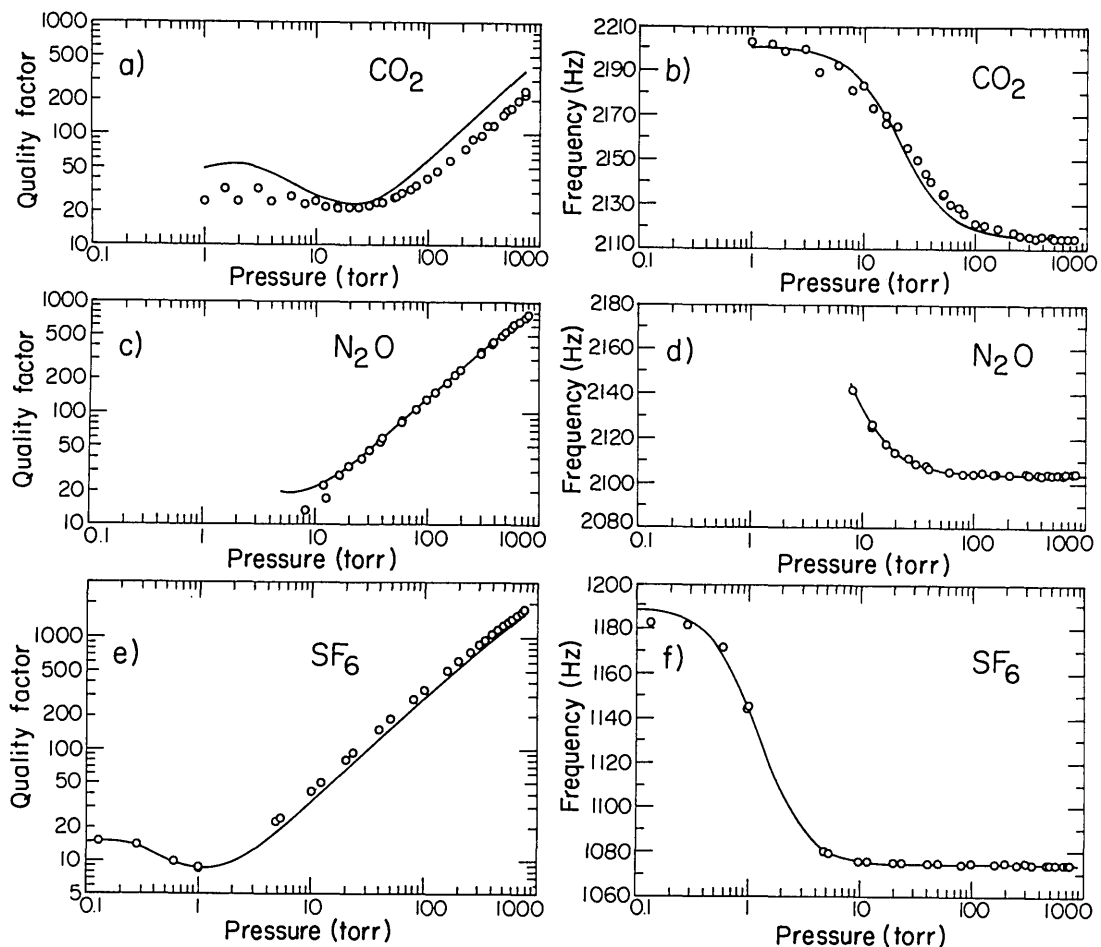

Fig. 7. Quality factor and first radial resonant frequency vs pressure for the polyatomic gases. Frequencies have been corrected by subtracting out virial and boundary layer shifts. Solid curves for frequency vs pressure graphs were obtained by curve-fitting frequency data to obtain a single relaxation time. Solid curves in Q vs pressure graphs were calculated by summing all losses, including relaxational losses calculated using the relaxation times obtained from the frequency data.

Here we find that calculated losses account for typically 95% of the observed losses for nonrelaxing gases, with no significant deterioration in the agreement for relaxing gases, due to the inclusion of relaxation in the calculated losses. We attribute this improvement in agreement with theory to

(1) use of a more complete theoretical description of the losses, including molecular relaxation effects;

(2) a reduction in the amount of doping gas added to give absorption of the laser light, resulting in less severe perturbation of the buffer gas properties;

(3) an improved surface finish in the resonator, giving a better-defined boundary layer whose behavior was more likely to agree with theory; and

(4) a cleaner cavity geometry, which eliminated losses that are hard to account for, such as scattering losses.

In the course of the study, we have also noted factors causing shifts in the resonant frequencies of the spectrophone due to boundary layer effects, virial shifts in the sound velocity, and dispersion due to molecular relaxation. These shifts can all be well accounted for theoretically.

The main discrepancies encountered occurred for CO_2, for which the calculated losses fell short of the observed losses by a greater amount and for which the observed relaxation time is much shorter than obtained by others.

We have gained some insight into the physics of the resonant spectrophone and hope that it will be of some use to other users of such detectors.

This paper was presented (in part) at the Second Topical Meeting on photoacoustic spectroscopy, Berkeley, 22–25 June 1981.

Appendix: Frequency Shift due to Boundary Layer

For a resonance having an unperturbed frequency ω_0, the perturbation due to boundary layer effects modifies the frequency to

$$\omega = \omega_0 + \delta\omega + i\Gamma, \qquad (A1)$$

where $\delta\omega$ is the shift in resonant frequency and Γ is the broadening of the resonance contributed by the perturbation. The perturbation in the frequency is given by[6]

$$\delta\omega + i\Gamma = i\frac{c}{2}\int_S \phi_n^2(\mathbf{r})\beta_b(\mathbf{r},\omega)dS \Big/ \int_V \phi_n^2(\mathbf{r})dV, \qquad (A2)$$

where $\phi_n(\mathbf{r})$ is the velocity potential function for the nth mode, and β_b is the specific acoustic admittance of the boundary layer. This admittance can be written as[13]

$$\beta_b = \xi_b + i\sigma_b, \qquad (A3)$$

where ξ_b and σ_b are the specific acoustic conductance and susceptance, respectively. For a plane wave incident on a plane surface at angle θ to the normal we have[4]

$$\xi_b = \sigma_b = \frac{\omega d_v}{2c}\sin^2\theta + (\gamma - 1)\frac{\omega d_h}{2c}. \qquad (A4)$$

For the case of a purely radial mode in a cylindrical resonator, the sound wave behaves like a normally incident plane wave along the side walls and like a wave propagating parallel to the surface along the end walls. Therefore,

$$\sin^2\theta = \begin{cases} 0 & \text{on side walls,} \\ 1 & \text{on end walls.} \end{cases} \qquad (A5)$$

For a purely radial mode,

$$\phi_n = J_0(\pi\alpha_{on}r/R). \qquad (A6)$$

Substitution of Eqs. (A3)–(A6) into Eq. (A2) and integration yield

$$\delta\omega = -\Gamma = -\frac{\omega}{2L}\left[d_v + (\gamma-1)d_h\left(1 + \frac{L}{R}\right)\right]. \qquad (A7)$$

Dividing through by ω yields Eq. (18). We note that by setting $Q = \omega/2\Gamma$ we reproduce Kamm's result for the quality factor of a radial mode.[3]

References

1. L. J. Thomas, M. J. Kelly, and N. M. Amer, Appl. Phys. Lett. **32**, 736 (1978). In Table I of this reference, the ratio Q_{exp}/Q_{cal} was based on incorrectly calculated values of Q_{cal}. The Q_{exp}/Q_{cal} column should read: Ne, 0.87; Ar, 0.77; Kr, 0.82; Xe, 0.76; CO, 0.73; N_2, 0.82; $^{12}CO_2$, 0.15; N_2O, 0.36; SF_6, 0.44.
2. P. M. Morse, *Vibration and Sound* (McGraw-Hill, New York, 1948).
3. R. D. Kamm, J. Appl. Phys. **47**, 3550 (1976).
4. P. M. Morse and K. U. Ingard, *Theoretical Acoustics* (McGraw-Hill, New York, 1968).
5. A. J. Matheson, *Molecular Acoustics* (Wiley-Interscience, London, 1971).
6. K. Frank and P. Hess, Chem. Phys. Lett. **68**, 540 (1979).
7. J. B. Mehl and M. R. Moldover, J. Chem. Phys. **74**, 4062 (1981).
8. E. G. Richardson, *Ultrasonic Physics* (Elsevier, Amsterdam, 1962).
9. The cell was constructed of type 304 stainless steel. It was later learned that type 316 stainless is more suitable for polishing.
10. J. R. Peele and T. J. Whitney, Rev. Sci. Instrum. **40**, 1114 (1969).
11. Thermal and transport properties of gases other than SF_6 were from Y. S. Touloukian and C. Y. Ho, Eds., *Thermophysical Properties of Matter*, Vols. 3 (1970), 6 (1970), and 11 (1975) (IFI/Plenum, New York). SF_6 data were from Landolt-Börnstein, *Zahlenwerte und Funktionen*, II Band, Teil 4 (1961), 5a (1969), and 5b (1968) (Springer, Berlin). Virial coefficients were from D. E. Gray, Ed., *American Institute of Physics Handbook* (McGraw-Hill, New York, 1972) except for N_2O and SF_6, which were from J. H. Dymond and E. B. Smith, *Virial Coefficients of Pure Gases and Mixtures* (Clarendon, Oxford, 1980). Molecular vibration frequencies used for the relaxation loss calculations were from G. Herzberg, *Molecular Spectra and Molecular Structure*, Vols. 1 (1950) (for H_2, N_2, O_2); 2 (1945) (for CO_2, N_2O), and 3 (1966) (for SF_6).
12. L. M. Valley and R. C. Amme, J. Chem. Phys. **50**, 3190 (1969).
13. We adopt the convention (consistent with Ref. 7) that harmonic quantities vary as $\exp(+i\omega t)$, leading to the definition in Eq. (A3). Reference 4 assumes an $\exp(-i\omega t)$ dependence, leading to their definition $\beta = \xi - i\sigma$.